CrossMark

Increasing the specific surface area of Cr-doped TiO$_2$ nanoparticles by controlling the drying time for DSSC applications

Morteza Asemi[1,2] · Abdollah Suddar[1,2] · Majid Ghanaatshoar[1,2]

Abstract In this work, in order to increase the efficiency of dye-sensitized solar cells (DSSCs), we synthesize Cr-doped TiO$_2$ nanoparticles by sol–gel method and study the influence of drying time in the Cr-doped TiO$_2$ nanoparticles preparation on the performance of the resultant DSSCs. The results show that the prepared sample at drying time of 18 h is composed of uniform nanoparticles with less aggregation in comparison with the other ones. In addition, specific surface area increases with the drying time of the nanoparticles and reaches the maximum value of 75.6 m^2/g and then starts to decrease. The DSSC fabricated from this sample exhibits a higher efficiency than those made from the nanoparticles with other drying times. The increase in efficiency is ascribed to the higher dye-loading of nanoparticles due to the high specific surface area which is verified by dye-loading and BET measurements. The charge recombination in the DSSCs has been also studied by electrochemical impedance spectroscopy.

1 Introduction

In recent years, dye-sensitized solar cells (DSSCs) have attracted a great deal of both scientific and industrial attention for sunlight to electricity conversion due to their relatively simple, inexpensive device fabrication and high power conversion efficiencies [1–3]. In general, a DSSC consists of a dye-sensitized photoelectrode, a liquid iodide electrolyte as redox couple, and a platinized counter electrode to collect electrons and catalyze the redox couple regeneration [4–6]. The dye-sensitized photoelectrode is composed of a mesoporous semiconductor oxide film on a transparent conducting oxide (TCO) substrate sensitized by a dye for absorbing visible light [7]. The dye-sensitized photoelectrode as the main component of a DSSC plays a vital role in the DSSC performance. The mesoporous semiconductor provides a substrate for dye adsorption, accepts electrons from the photoexcited dye molecules and transports the electrons towards the transparent conducting oxide [8, 9]. Therefore, in order to achieve high performance DSSCs, we require semiconductor electrodes with high surface area to provide sufficient photosensitive dye adsorption, suitable conduction band edge that matches the LUMO level of the dye molecules and fast electron transport or long electron lifetime [10, 11].

Until now, many semiconductors such as TiO$_2$, ZnO and SnO$_2$ have been used as photoanode materials to improve the efficiency of DSSCs, [12–14]. Apparently, TiO$_2$ has been demonstrated to be the best semiconductor electrode material due to its excellent chemical and physical properties [15, 16]. Subsequently, various methods have been investigated to enhance the efficiency of the DSSCs by improving the TiO$_2$ properties, such as changing TiO$_2$ particles morphology and crystallographic structure (for example, the electron transport of the anatase phase is better than that of the rutile phase), by performing heat treatment on TiO$_2$ particles and introducing metal dopants [17]. In recent years, a great deal of attention has been paid to the doped TiO$_2$ nanostructures to enhance the photovoltaic performance. Nikolay et al. found an increase in the short circuit current of DSSCs fabricated with Nb-doped TiO$_2$ electrode [18]. Zhang et al. reported an increase in the

✉ Majid Ghanaatshoar
   m-ghanaat@sbu.ac.ir

[1] Laser and Plasma Research Institute, Shahid Beheshti University, G.C., Evin, Tehran 1983969411, Iran

[2] Solar Cells Research Group, Shahid Beheshti University, G.C., Evin, Tehran 1983969411, Iran

efficiency of DSSCs fabricated with Zn- and W-doped TiO$_2$ nanorod arrays [19]. Recently, the doping of TiO$_2$ nanoparticles with Cr ions has attracted attention because this ion can excellently extend the visible light absorption and improve the photocatalytic activity of TiO$_2$ [20, 21]. Xie et al. exploited Cr-doped TiO$_2$ nanoparticles in photoanode of DSSCs and investigated the effect of Cr doping on their photovoltaic properties [22]. Efficiency improvement of the DSSCs by Cr-doped TiO$_2$ photoanodes was also done by Mohammadi et al. [23]. Cr dopant incorporated into TiO$_2$ crystal lattice can form an impurity energy level within the TiO$_2$ bandgap, which allows photons with some lower energy to excite photocatalyst to exhibit visible light activity [24]. The light-harvesting improvement (and the consequent increase of charge carrier concentration) facilitates the electron-transfer and leads to enhancement of the photocurrent density.

Besides the aforementioned improvement, increasing the porosity and specific surface area of the nanoparticles is essential to achieve the highest value of short circuit current density and power conversion efficiency. In most studies, increasing the specific surface area is mainly limited to TiO$_2$ micro/nanostructures. Previously, well-crystallized mesoporous anatase TiO$_2$ spheres were prepared by hydrothermal treatment of the titanium diglycolate precursors. These spheres were submicrometer-sized and consisted of packed nanocrystallites with diameters of about 8 nm [25]. Subsequently, TiO$_2$ nanofibers for use in DSSCs were prepared from a solution of polymerized titanium tetraisopropoxide using a modified electro-spinning process to create fibers with high specific surface areas [26]. Then, He et al. synthesized TiO$_2$ porous nanotubes by coating a porous layer on the walls of the TiO$_2$ nanotubes. The coating of TiO$_2$ layers on nanotube walls effectively improved the specific surface area [27]. Recently, hierarchical mesoporous TiO$_2$ submicro/nanostructured spheres with high specific surface area were prepared by water heating reflux of hydrolyzed TiO$_2$ precursors of organic titanium [28]. Furthermore, Guo et al. prepared novel one-dimensional anatase hierarchical TiO$_2$ submicrorods with higher specific surface area than P25 nanoparticles [29].

In the present work, in order to increase the efficiency of DSSCs, we synthesize Cr-doped TiO$_2$ nanoparticles by sol–gel method and study the influence of the drying time on the properties of the prepared nanoparticles. The change in porosity and specific surface area of the synthesized nanoparticles are related to the duration of the drying time of the TiO$_2$ nanopowders. In fact, during the drying process, the organic residues are removed from the nanoparticles and leave a pore structure [30]. Nanoparticles with high porosity and specific surface area are desirable for loading a large amount of the dye and subsequently increasing the efficiency of the DSSCs due to the more light-harvesting.

Investigation of photovoltaic properties of the DSSCs constructed from the synthesized Cr-doped TiO$_2$ nanoparticles will reflect the influence of the drying time duration.

2 Experimental details

For the preparation of Cr-doped TiO$_2$ nanoparticles (0.5%), sol–gel method was used. Firstly, an appropriate value of chromium nitrate nonahydrate (Cr(NO$_3$)$_3$.9H$_2$O, Merck Co., Germany) was dissolved in 60 ml of deionized water (solution A). The pH of solution A was adjusted with acetic acid (AcOH, Merck Co., Germany) to 2. Then, solution B was prepared by slowly adding 0.05 mol of titanium tetraisopropoxide (TTIP, Samchun Chemical Co., Korea) to 40 ml ethanol (EtOH, Amertat Shimi Co., Iran) at room temperature at vigorous stirring. Solution B was added to solution A at vigorous stirring and stirred for 2 h at room temperature. The obtained solution was aged at room temperature for 48 h. In order to investigate the effect of the drying time on the properties of nanoparticles, the resulting gel was dried at 80 °C for 6, 12, 18 and 24 h. Finally, the obtained powders were ground and annealed at 450 °C for 2 h in a laboratory electric furnace (Azar Furnace Co., Model F35L-1200, Iran).

TiO$_2$ pastes of various samples were deposited on the fluorine-doped tin oxide (FTO) glass (2.2 mm thickness, 20 Ω/sq) through doctor blade method. In order to sinter and obtain the mesoporous structure, the prepared TiO$_2$ films were gradually heated at 450 °C for 30 min. After cooling down to 80 °C, the resulting mesoporous TiO$_2$ working electrodes were immersed into a 0.4 mM ethanolic solution of N719 dye (Dyesol Co., Australia) and were kept for 24 h in the dark. Subsequently, the dye-loaded mesoporous TiO$_2$ electrode and Pt-counter electrode were assembled into a sandwich type DSSC configuration. The space between two electrodes was filled with a liquid electrolyte consisting of 0.5 M LiI and 0.05 M I$_2$ in acetonitrile. The active area of each cell was fixed at 0.2 cm^2.

To determine the crystalline structure and crystallite size of the prepared Cr-doped TiO$_2$ nanoparticles, X-ray diffraction (XRD) patterns were recorded by using a PANalytical X'Pert Pro Powder Diffractometer with Cu Kα radiation (λ = 1.54016 Å). The particle size and morphology of the prepared Cr-doped TiO$_2$ nanoparticles were investigated by using a field emission scanning electron microscope (FESEM, TESCAN mira 3 xmu, Czech Republic). The Brunauer–Emmett–Teller (BET) analysis was also performed using a Belsorp mini II instrument (BelJapan, Japan) to determine the specific surface area and porosity of the nanoparticles. The current–voltage characteristic curves of the constructed DSSCs were obtained by applying an external potential bias to the device and measuring

the generated photocurrent with an I-V tracer (IV-25, Sharif Solar, Iran) under illumination of an AM1.5 solar simulator (SIM-1000, Sharif Solar, Iran). To determine the amount of the dye absorbed on Cr-doped TiO_2 nanoparticles, the dyes were desorbed from Cr-doped TiO_2 photoelectrodes using 0.1 M NaOH solution and the absorbance of the solution was measured by using a UV–Vis spectrophotometer (3648 UV–Vis, Avantes, Netherlands). In order to investigate the charge recombination kinetics in the prepared DSSCs, the electrochemical impedance spectroscopy (EIS) was carried out using a potentiostat/galvanostat (IVIUM, Compactstat, Ivium Technologies BV, Netherlands) by applying bias of the open-circuit voltage under illumination of 100 mW/cm^2 in frequency range of 0.1 Hz–100 kHz with a perturbation amplitude of 10 mV.

3 Results and discussion

The XRD patterns of the Cr-doped TiO_2 nanoparticles synthesized by the sol–gel method are shown in Fig. 1. In order to facilitate comparison, the samples dried in 6, 12, 18 and 24 h are named CT6, CT12, CT18 and CT24, respectively. All the peaks in the XRD patterns can be attributed to the tetragonal structure of TiO_2 with anatase phase which is in agreement with the data obtained from JCPDS File No. 21-1272. For the dopant concentration used in the present work, there is no effect of the Cr dopant on the crystal structure. Our results are in agreement with results reported by other authors [20, 31]. The XRD patterns indicate that the drying time has slightly influenced the crystallite size of the prepared Cr-doped TiO_2 nanoparticles.
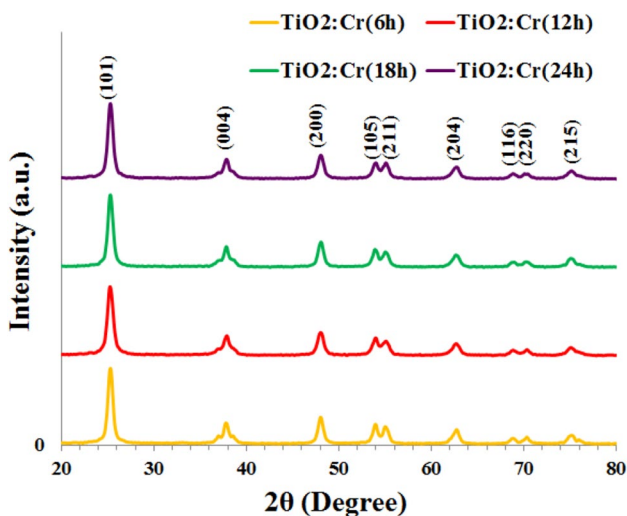

Fig. 1 XRD patterns of the synthetized Cr-doped TiO_2 nanoparticles at different drying time durations

We employ the Debye–Scherrer equation to evaluate the crystallite size from the XRD data by determining the width of the (101) Bragg diffraction peak. The Debye–Scherrer equation is expressed as [32]:

$$d_{hkl} = \frac{0.9\,\lambda}{\beta \cos\,(\theta)}$$

where d_{hkl} represents the crystallite size in the direction of the (hkl) plane, β is the full width at half maximum of the (hkl) diffraction peak in radians and λ is around 0.154 nm. By this equation, the crystallite size of the Cr-doped TiO_2 nanoparticles is found to be about 11.3 nm for CT6, CT12 and CT24 and about 12.5 nm for CT18, respectively. These results clearly show that the crystallite size of the CT18 sample is different from those of the other three samples. Previously, Hsiang et al. observed that the crystallization of anatase phase for TiO_2 gel obtained from $TiCl_4$ was promoted with the aging process and the crystallinity of the anatase phase increased with increasing the aging time [33]. Our results are in agreement with their observation.

The FESEM images of the synthesized nanoparticles are shown in Fig. 2. As can be seen from this figure, the size of the nanoparticles is about 10–20 nm for all the samples. The morphology and the shape of CT6, CT12 and CT24 nanoparticles are the same and the nanoparticles are aggregated in these samples. In contrast, the morphology and the shape of CT18 nanoparticles are obviously different. This sample is composed of fine and discrete nanoparticles with good uniformity and without any aggregation. In most of the previous works, annealing of TiO_2 nanoparticles at high temperatures led to aggregation of prepared nanoparticles [34]. Previously, peptization in the presence of nitric acid was used by Vorkapic et al. to break up the aggregates into very small aggregates less than 20 nm [35]. In order to prevent the aggregation and sintering of the TiO_2 nanoparticles, Cong et al. synthesized nitrogen-doped TiO_2 nanoparticles by microemulsion-hydrothermal method under nitric or hydrochloric acid environment [36]. As we know, hydrothermal synthesis method is carried out at the temperature of 100–200 °C. Our results indicate that by controlling the drying time, we can hinder the aggregation of the nanoparticles during the synthesizing process. The obtained discrete Cr-doped TiO_2 nanoparticles with uniform size can be attributed to the reduction of the existing hydroxyl ions in the anatase lattice by controlling the drying time [33].

During the drying process, the organic residues are removed from the nanoparticles and a pore structure is created [37]. We expect that with increasing the drying time, the specific surface area of the nanoparticles changes. In order to study the porosity of the prepared Cr-doped TiO_2 nanoparticles, Brunauer–Emmett–Teller (BET) analysis was performed. The specific surface area, pore volume and pore diameter of the prepared Cr-doped TiO_2 nanoparticles
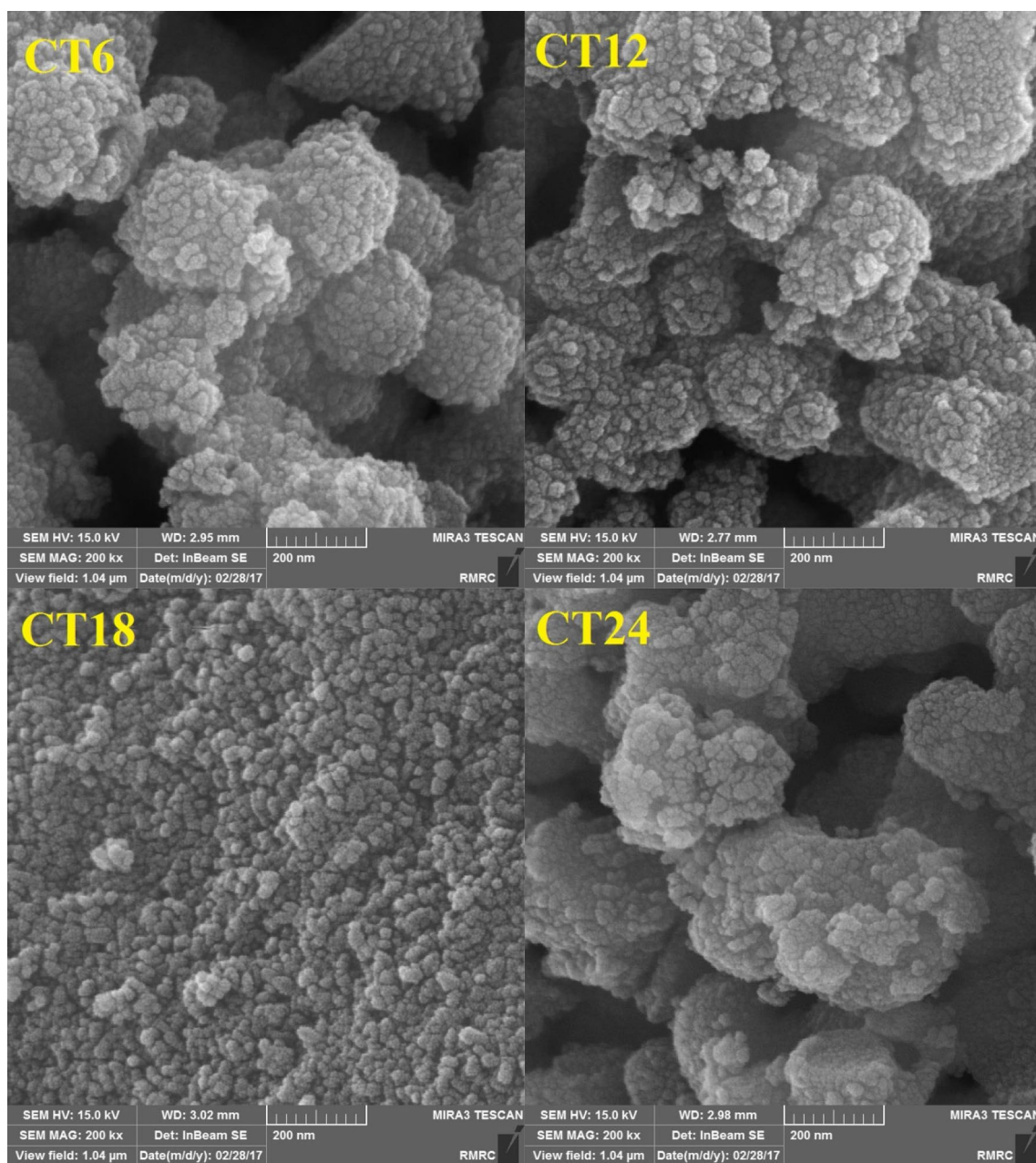
Fig. 2 FESEM images of the synthetized Cr-doped TiO$_2$ nanoparticles

are exhibited in Table 1. As can be seen, the specific surface area increases from 46.4 m^2/g (for the sample CT6) to 75.6 m^2/g (for the sample CT18) and then decreases to 56. 4 m^2/g (for the sample CT24). The increased surface area of CT18 can be helpful to improve the surface reaction of the nanoparticles and dye loading in comparison with CT6 nanoparticles [38]. The obtained results are in good agreement with FESEM images of TiO$_2$ nanoparticles. The results confirm that the discrete TiO$_2$ nanoparticles have higher specific surface area than the aggregated ones. These results also highlight the significant improvement

Table 1 The results of the BET analysis of the prepared nanoparticles

Sample	Pore diameter (nm)	Specific surface area (m^2/g)	Pore volume (cm^3/g)
CT6	10.8	46.4	0.125
CT12	8.9	69.1	0.153
CT18	8.6	75.6	0.136
CT24	9.4	56.4	0.132

in the specific surface area of the TiO$_2$ nanoparticles that can be achieved by controlling the drying time during the sol–gel process.

The photocurrent density–voltage (J–V) characteristics of the Cr-doped TiO$_2$ DSSCs made from Cr-doped TiO$_2$ nanoparticles are illustrated in Fig. 3. The corresponding photovoltaic parameters such as short circuit current (J_{SC}), open circuit voltage (V_{OC}), fill factor (FF) and power conversion efficiency (η) are also listed in Table 2. In order to have a direct comparison, we consider the same thickness for the devices. It can be seen that increasing the drying time of the nanoparticles firstly increases the short circuit current density (J_{SC}) from 6.48 mA/cm^2 (CT6-DSSC) to 12.40 mA/cm^2 (CT18-DSSC), and then decreases to 4.28 mA/cm^2 (CT24-DSSC). Similar behavior is observed in power conversion efficiency. The maximum efficiency is obtained for CT18-DSSC (2.97%). Obviously, the enhanced performance of CT18-DSSC is mainly associated with a remarkable increase in J_{SC}. In our case, the increment in J_{SC} of CT18-DSSC can be ascribed to the higher specific surface area of CT18 nanoparticles in comparison with the other ones which was previously confirmed by the BET experiment. Nanoparticles with higher specific surface area and porosity are desirable for dye-loading [39, 40]. In order to verify the effect of specific surface area on the J_{SC}, dye-loading measurement was carried out. The dye-loading measurement was performed by desorbing the dye in 1 mM NaOH aqueous solution and measuring the UV–visible absorption spectrum [41]. The results show an improvement in dye absorption for the DSSC made from CT18 nanoparticles (CT18-DSSC), as shown in Fig. 4. The higher dye-loading in CT18-DSSC is due to the larger specific surface area of the nanoparticles which in turn, leads

Table 2 Photovoltaic properties of the fabricated DSSCs

Photoanode	J_{SC} (mA cm^{-2})	V_{OC} (mV)	FF	η(%)
CT6	6.48	546	0.52	2.33
CT12	8.00	496	0.48	2.37
CT18	12.40	476	0.40	2.97
CT24	4.28	585	0.58	1.84

to the better performance of the DSSC made from CT18 nanoparticles.

The decrease in the value of the V_{OC} with increasing the drying time can also be attributed to the higher specific surface area and porosity of the nanoparticles. Due to having higher surface activity, nanoparticles with higher specific surface area suffer from a higher degree of charge recombination, i.e., the open-circuit voltage decreases with increasing the specific surface area. In order to elucidate the influence of the specific surface area on the charge recombination resistance, the electrochemical impedance spectroscopy was carried out in the frequency range between 0.1 Hz and 100 kHz with an ac-voltage amplitude of 10 mV at the open-circuit potential [42]. The first arc in the high frequency region (left hand side) represents charge transport resistance at the counter electrode/electrolyte interface or FTO/photoanode interface (R_1), and the second arc in the intermediate frequency region (right hand side) represents electron recombination resistance at the photoanode/electrolyte interface (R_2). The size of the second arc (R_2) is an important factor which affects the photovoltaic performance. As can be seen from Fig. 5, the CT18-DSSC exhibits an electron recombination resistance value of 68 Ω, which is significantly smaller than the other ones,
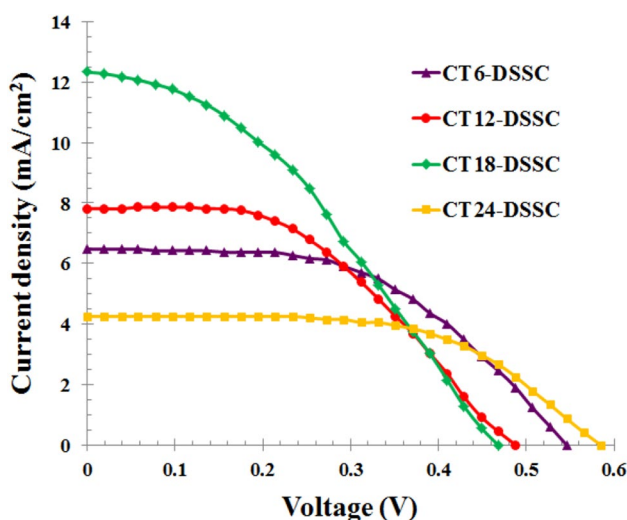

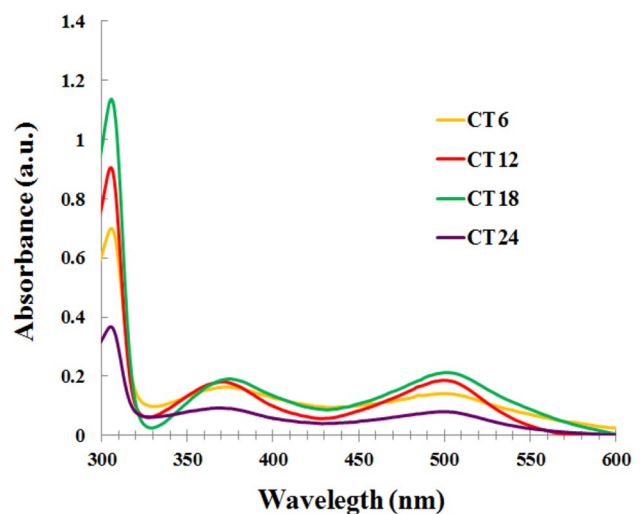**Fig. 3** Current density–voltage curves of the fabricated DSSCs

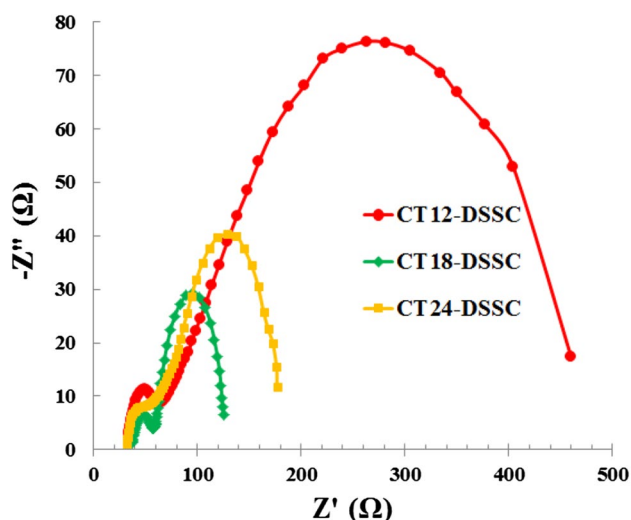**Fig. 4** UV–vis absorption spectra of N719 dye desorbed from Cr-doped TiO$_2$ photoanodes

Fig. 5 Nyquist plots of the fabricated Cr-doped TiO_2-based DSSCs

signifying fast recombination reaction in this device. Due to having a larger surface area in comparison with the other prepared nanoparticles, the particles dried for 18 h have more trapping sites which facilitate the charge recombination with I_3^- in the electrolyte [43]. Regarding the efficiency enhancement, we conclude that in CT18-DSSC, the effect of the specific surface area on the J_{SC} improvement is predominant in comparison with V_{OC} reduction.

4 Conclusions

Cr-doped TiO_2 nanoparticles were prepared by sol–gel method. It was shown that the time of drying influences the size and porosity of the nanoparticles. Furthermore, the efficiency of the constructed DSSCs was improved by managing the drying time of the Cr-doped TiO_2 nanoparticles and reached the maximum of 2.97%. This improvement in the efficiency was attributed to the enhancement of the surface area which enables higher dye-loading and light-harvesting. In addition, EIS measurement revealed that the charge recombination resistance of the fabricated DSSC with CT18-DSSC is smaller than that of the other ones due to the larger surface area. The trade-off between the change in J_{SC} and V_{OC} by the specific surface area determines the amount of the efficiency enhancement.

References

1. S. Shogh, R. Mohammadpour, A. Iraji zad, N. Taghavinia, Appl. Phys. A **119**, 1283 (2015)
2. J. Liu, A. Wei, Y. Zhao, K. Lin, F. Luo, J. Mater. Sci. **25**, 1122 (2014)
3. M. Asemi, M. Ghanaatshoar, J. Mater. Sci. **52**, 489 (2017)
4. S.M. Yong, N. Tsvetkov, L. Larina, B.T. Ahn, D.K. Kim, Thin Solid Films **556**, 503 (2014)
5. H.C. Hung, Y.J. Lin, Z.Y. Ke, J. Mater. Sci. **27**, 5059 (2016)
6. M. Asemi, M. Ghanaatshoar, Ceram. Int. **42**, 6664 (2016)
7. B. Liu, E.S. Aydil, Renew. Sust. Energy **3**, 043106 (2011)
8. T.K. Yun, S.S. Park, D. Kim, Y.K. Hwang, S. Huh, J.Y. Bae, Y.S. Won, J. Power Sources **196**, 3678 (2011)
9. J. Bandara, U.W. Pradeep, Thin Solid Films **517**, 952 (2008)
10. B. Juan, C. David, H. Gary, R. Sven, Z. Arie, J. Phys. Chem. B **108**, 8106 (2004)
11. J. Liua, H. Yanga, W. Tana, X. Zhoua, Y. Lin, Electrochim. Acta **56**, 396 (2010)
12. M. Pazoki, N. Taghavinia, Y. Abdi, F. Tajabadi, G. Boschloo, A. Hagfeldt, RSC Adv. **2**, 12278 (2012)
13. M. Saleem, L. Fang, S.F. Shaukat, M.A. Ahmad, R. Raza, M.N. Akhtar, A. Jamil, S. Aslam, G. Abbas, Appl. Surf. Sci **334**, 145 (2015)
14. M. Abrari, M. Ghanaatshoar, S.S.H. Davarani, H.R. Moazami, I. Kazeminezhad, Appl. Phys. A **123**, 326 (2017)
15. J. Yan, F. Zhou, J. Mater. Chem. **21**, 9406 (2011)
16. Q.P. Liu, Electrochim. Acta **129**, 459 (2014)
17. M. Asemi, M. Ghanaatshoar, Appl. Phys. A **122**, 853 (2016)
18. T. Nikolay, L. Larina, O. Shevaleevskiy, B.T. Ahn, Energy Environ. Sci. **4**, 1480 (2011)
19. X. Zhang, S.T. Wang, Z.S. Wang, Appl. Phys. Lett. **9**, 113503 (2011)
20. C. Wang, H. Shi, Y. Li, Appl. Surf. Sci. **258**, 4328 (2012)
21. B. Tian, C. Li, J. Zhang, Chem. Eng. J. **15**, 402 (2012)
22. Y. Xie, N. Huang, S. You, Y. Liu, B. Sebo, L. Liang, X. Fang, W. Liu, S. Guo, X.Z. Zhao, J. Power Sources **224**, 168 (2013)
23. M.R. Mohammadi, A.M. Bakhshayesh, F. Sadri, M. Masroor, J. Sol-Gel Sci. Technol. **67**, 77 (2013)
24. Y.H. Peng, G.F. Huang, W.Q. Huang, Adv. Powder Technol. **23**, 8 (2012)
25. W.G. Yang, F.R. Wan, Q.W. Chen, J.J. Lia, D.S. Xu, J. Mater. Chem. **20**, 2870 (2010)
26. W.H. Jung, N.S. Kwak, T.S. Hwang, B. Yi, Appl. Surf. Sci. **261**, 343 (2012)
27. W. He, J. Qiuf, S.K. Choi, W.D. Kim, J.H. Lee, Y.D. Kime, S.H. Kimg, H.K. Kim, Y.H. Hwang, Curr. Appl. Phys. **11**, 320 (2011)
28. J. Liu, Q. Zhang, L. Niu, B. Hu, X. Zhou, J. Mater. Sci. **27**, 9115 (2016)
29. D. Guo, S. Xiao, K. Fan, J. Yu, ACS Sustain. Chem. Eng. **5**, 1315 (2017)
30. N. Job, A. Thery, R. Pirard, J. Marien, L. Kocon, J.N. Rouzaud, F. Beguin, J.P. Pirard, Carbon **43**, 2481 (2005)
31. Z. Hong, T. Jie, D. Xiang, J. Phys. Chem. C **114**, 2873 (2010)
32. M. Asemi, M. Ghanaatshoar, J. Sol-Gel Sci. Technol. **70**, 416 (2014)
33. H.I. Hsiang, S.C. Lin, Mater. Sci. Eng. A **380**, 67 (2004)
34. B. Choudhury, A. Choudhury, Int. Nano Lett. **3**, 55 (2013)
35. D. Vorkapic, T. Matsoukas, J. Am. Ceram. Soc. **81**, 2815 (1998)
36. Y. Cong, J. Zhang, F. Chen, M. Anpo, J. Phys. Chem. C **111**, 6976 (2007)
37. M. Pelaez, A. Armah, E. Stathatos, P. Falaras, D.D. Dionysiou, Catal. Today **14**, 19 (2009)
38. M. Khalid, J.S. Hyung, J. Mater. Chem. A **2**, 5408 (2014)
39. M.C. Kao, H.Z. Chen, S.L. Young, C.Y. Kung, C.C. Lin, Thin Solid Films **517**, 5096 (2009)
40. W. Wang, H. Zhang, R. Wang, M. Feng, Y. Chen, Nanoscale **6**, 2390 (2014)
41. M. Asemi, M Ghanaatshoar Appl. Phys. A **122**, 842 (2016)
42. M. Asemi, S. Maleki, M. Ghanaatshoar, J. Sol-Gel Sci. Technol **81**, 645 (2017)
43. A.H. Saif, T. Yasuhiro, L.W. Richard, E.M. Jacques, G. Michael, R.K. David, R.D. James, J. Phys. Chem. B **104**, 538 (2000)